CCFE
CULHAM CENTRE FOR FUSION ENERGY

UK Atomic Energy Authority

UKAEA-CCFE-PR(20)81

Allan HarteHuw DawsonDavid BowdenSimon KirkMike Gorley

Deformation heterogeneity in laser-welded Eurofer

Enquiries about copyright and reproduction should in the first instance be addressed to the UKAEA Publications Officer, Culham Science Centre, Building K1/0/83 Abingdon, Oxfordshire, OX14 3DB, UK. The United Kingdom Atomic Energy Authority is the copyright holder.

The contents of this document and all other UKAEA Preprints, Reports and Conference Papers are available to view online free at scientific-publications.ukaea.uk/

Deformation heterogeneity in laser-welded Eurofer

Allan HarteHuw DawsonDavid BowdenSimon KirkMike Gorley

This is a preprint of a paper submitted for publication in
Fusion Engineering and Design

CCFE
CULHAM CENTRE FOR FUSION ENERGY

UK Atomic Energy Authority

UKAEA-CCFE-PR(20)81

Allan Harte Huw Dawson David Bowden Simon Kirk
Mike Gorley

Deformation heterogeneity in laser-welded Eurofer

Enquiries about copyright and reproduction should in the first instance be addressed to the UKAEA Publications Officer, Culham Science Centre, Building K1/0/83 Abingdon, Oxfordshire, OX14 3DB, UK. The United Kingdom Atomic Energy Authority is the copyright holder.

The contents of this document and all other UKAEA Preprints, Reports and Conference Papers are available to view online free at https://scientific-publications.ukaea.uk/

Deformation heterogeneity in laser-welded Eurofer

Allan Harte Huw Dawson David Bowden Simon Kirk Mike Gorley

This is a preprint of a paper submitted for publication in
Fusion Engineering and Design

UKAEA, 2019

Deformation heterogeneity in laser-welded Eurofer

Allan Harte, Huw Dawson, David Bowden, Rory Spencer, Simon Kirk, Michael Gorley

Keywords: DEMO; laser weld; Eurofer; RAFM steel; digital image correlation; PWHT; deformation; heat treatment; mechanical testing; fusion

Abstract

The suitability of post-weld heat treatments are often measured in terms of reducing residual stress and/or ensuring hardness homogeneity. Here we use detailed digital image correlation to quantify the localised deformation behaviour of laser welded Eurofer-97 both with and without a normalising and tempering treatment. This is coupled with detailed microscopic analysis to investigate the mechanisms for the localised plasticity measured. We show that although the treatment ensures hardness homogeneity, there remains variation in grain size, texture, carbide morphology/density and tensile behaviour across the weld. A quantification of strain heterogeneity throughout the test provides a new measure of performance that indicates the suitability of both microstructure and macroscopic performance for engineering applications.

1 Introduction

Localised strain heterogeneity is a precursor to failure [1,2] and full-field strain mapping techniques such as digital image correlation (DIC) are able to quantify local deformation for a better understanding of failure mechanisms. The performance of welded sections in ferritic-martensitic steel has primarily concerned its creep behaviour and the understanding of Type IV cracking [3–6]. For Eurofer-97 [7], and its non-reduced activation analogue Grade 91 steel, post-weld heat treatments (PWHTs) have been optimised towards reducing residual stresses and hardness variation across the weld [8–11] and, to some degree, towards improving mechanical performance, for instance Charpy toughness [12] and creep rupture [13]. Measuring and understanding the full-field deformation behaviour of a heterogeneous component provides quantitative data that can be used to optimise PWHTs and to validate numerical models of larger components with welds, improving their accuracy and reducing conservatism in design. Such an approach could have wide implications for design codes and regulations.

DIC is well-suited to the analysis of highly heterogeneous components such as welds. DIC has been used to observe high creep strain localisation in the heat-affected zone of welded Grade 91 steel as a precursor to Type IV cracking [14] and DIC has been used to understand zone-dependent strain localisation under tension in F82H [15]. While DIC has been used effectively to extract zone-specific data over welds in steels [16–18] and titanium alloys [19], the full-field data in such studies lacks spatial resolution and is not understood in terms of the underlying microstructure. The purpose of this work is to bridge this gap by determining the suitability of a PWHT in terms of its tensile performance. We do this by applying DIC with sufficient lateral resolution to investigate local plastic phenomena as the mesoscopic scale and parallel detailed electron microscopy to investigate the underlying deformation mechanisms. Importantly, we demonstrate that homogeneity in hardness is a useful tool but does not necessarily correspond to homogeneity in microstructure nor tensile deformation behaviour.

2 Experimental

2.1 Material, welding, heat treatment and preparation for testing

The material studied here is Eurofer-97 (batch 2) 6 mm-thick plate with composition (wt.%, balance Fe): 0.11 C, 8.7 Cr, 1 W, 0.10 Ta, 0.19 V, 0.44 Mn, 0.004 S [20]. Autogenous square butt welds were produced from two 6 mm-thick plates using a laser keyhole welding process using a continuous wave 1060 nm wavelength Ytterbium fibre laser source operating at 6 kW with a 0.6 mm diameter spot and a weld speed of 0.5 mm min^{-1}. A 200 mm focal length was used with the focal point at the top of the weld. The welds used in this work where taken from Weld C from Kirk et al. (2018) [21]. This laser welded (LW) piece was machined by EDM in cross section into the micro tensile geometry shown in Figure 1. The following normalising and tempering heat treatment was performed on microtensile specimens both with a LW and on microtensile specimens machined from the base material without a LW: Normalise above the first austenitic transformation temperature at 1050 °C for 40 min; Air cool to room temperature; Temper at 760 °C for 120 min; Air cool to room temperature. The austenitic phase transformation and associated volumetric change mean that the use of this heat treatment in engineering application would be limited. However, it is the most likely to create the most uniform microstructure variation possible across the weld and so it was chosen for the purposes of demonstration.

In preparation for hardness measurements, electron microscopy and digital image correlation, the microtensile specimens were polished to a mirror finish to ensure a deformation-free surface from which to extract materials property data. Four specimen types (with/without a weld and pre/post heat treatment) were prepared by mechanical grinding to remove the EDM recast layer and oxidation layer (removal of approximately 0.15 mm of material from the specimen surface) with SiC paper grades P800 and P1200 and then mechanical polishing to a mirror finish by grinding with successively finer grit SiC paper P2500 and P4000 and then diamond polishing at 6 μm and 1 μm before polishing with 60 nm colloidal silica particles for the mirror finish.

2.2 Mechanical testing and digital image correlation

Microhardness measurements were carried out on the base material, as-welded and heat treated conditions on a Leco LM 100AT automated microhardness tester. A load of 500 grams (HV0.5) was used with a dwell time of 10s. Indents were taken across the cross sections of the as-welded and heat-treated weld specimens. Indents were spaced at 400 μm intervals in both the vertical and the horizontal. The measured indents were used to produce microhardness colourmaps using OriginPro software. For the measure of hardness in the base material, nine indents were performed in a 3×3 grid with 2 mm spacings from a non-welded Eurofer-97 plate. The orientation was the same as the cross section of the weld.

Digital image correlation (DIC) requires features from which to track displacements in order to calculate strain. Here we have used a combination of black ink and white paint to produce a speckle pattern on the surface of the prepared microtensile specimens. Blank ink was used as the base layer because ink has no mechanical properties and will therefore deform easily with the material. The black ink was applied directly to the polished surface and left to dry. Fine white speckles were then applied to the black surface using white VITCAS® heat resistant paint and an Airbrush kit. The Airbrush kit consists of an air compressor and a paint gun that uses a 0.5 mm diameter needle to produce a fine spray of paint. The finest speckles possible were obtained with a compressor pressure of approximately 1.5 bar and minimum paint feed into the gun.

Speckle pattern quality is essential for good tracking of speckles during DIC. The speckle pattern quality can be assessed by the Shannon entropy of the pattern, such that a higher entropy corresponds to a reduced uncertainty introduced during the correlation, as shown by Liu et al. [22]. The Shannon entropy is defined as in Equation (1),

$$H = -\sum_{j=0}^{2^{\beta}-1} p(a_j)\log_2\left(p(a_j)\right) \quad \#(1)$$

where β is the bit depth of the image (12 for the current set up), $p(a_j)$ is the normalised probability of each grey level in the region of interest (calculated from the histogram of the region of interest) and j is each gray level. For all specimens in this work, the pattern entropy was within 7.44 ±0.07 bits px^{-1}, demonstrating a consistent patterning method and corresponding to the higher quality patterns determined by Liu et al. [22].

The DIC algorithm works by tracking grey level intensities within a subset of pixels, the size of which is selected by the operator. Uncertainty in the resulting displacement maps therefore depend on the accuracy of the algorithm in performing this function. As suggested by the iDIC guide for good quality DIC experiments [23], uncertainty in the measurement of strain was understood by way of a noise floor analysis, performed by capturing static images of the specimen under no load and calculating the strain field to quantify the pseudo-deformation due to random noise; with no applied load, there will be no deformation and hence any measured deformations can be assumed to be erroneous. Larger subsets decrease uncertainty, as they contain more distinct features, at the expense of spatial resolution. Therefore, an analysis of noise floor uncertainty with respect to the subset size allows the operator to determine the appropriate subset size for the correlation procedure and to determine the minimum uncertainty of the DIC measurements. This analysis is shown for one of the specimens in the present work in Figure 2, in which a subset size of 25 × 25 pixels was found to be optimal as this allowed all subsets to be correlated and any further increase in subset size provided limited decrease in uncertainty. The mean noise floor was approximately 0.014 % strain across all strain components and so this is our uncertainty in the measure of strain.

The microtensile specimens were gripped with cut-away holds on a 10 kN Intron 5966 and deformed in uniaxial tension to failure at a constant crosshead displacement rate of 0.005 mm s^{-1}. As all specimens were prepared to approximately the same thickness, the initial strain rates are comparable.

Full-field DIC was performed throughout each tensile test using LaVision's DaVis 10 software version 10.0.5.46211 using the least squares method and the parameters defined in Table 1.

The strains $\frac{\partial u_i}{\partial x_j}$ are calculated from the gradient of the displacements u_i (i = 1,2,3) along the principle directions x_i (i = 1,2,3), resulting in a n = 3 matrix of strain components. The measurements in this work are two-dimensional resulting in a n = 2 matrix for the strain field.

$$\frac{\partial u_i}{\partial x_j} = \begin{bmatrix} \frac{\partial u_1}{\partial x_1} & \frac{\partial u_2}{\partial x_1} \\ \frac{\partial u_1}{\partial x_2} & \frac{\partial u_2}{\partial x_2} \end{bmatrix} \#(2)$$

The maximum shear strain, ε_{MS}, can be a useful measure of effective strain because it reduces the vectoral field to a scalar and takes into account all of the in-plane components of the field [24].

$$\varepsilon_{MS} = \sqrt{\frac{1}{2}\left(\frac{\partial u_1}{\partial x_1} - \frac{\partial u_2}{\partial x_2}\right)^2 + \frac{1}{2}\left(\frac{\partial u_1}{\partial x_2} + \frac{\partial u_2}{\partial x_1}\right)^2} \quad \#(3)$$

The rotational component ω_3 can be used to visualise heterogeneity in the shear strain field, as it takes into account all of the in-plane shear components.

$$\omega_3 = \frac{\partial u_2}{\partial x_1} - \frac{\partial u_1}{\partial x_2} \#(4)$$

Strain data can be obtained from the full-field strain maps in different ways. The simplest way is to create a virtual extensometer that is a direct comparison to a physical one-dimensional clip-on extensometer, which works by tracking a subset of pixels at the top and bottom of a defined length, calculating the displacement between the two subsets and differentiating the displacement along the direction of the line to obtain strain. A second way to extract strain is by defining a two-dimensional spatial area of interest and taking the average (mean) of the strain values in that region. We use both methods in this work.

Displacement and strain data were exported from the DaVis software and manipulated by pythonic routines that used Numpy [25] libraries for mathematics and Matplotlib [26] for visualisation. All data is available for download [27].

2.3 Characterisation

A LaB_6 Zeiss Evo-60 scanning electron microscope (SEM) was used for microscopic analyses. Backscattered electron (BSE) imaging was performed with a standard Zeiss BSE detector at 8 kV and 500 pA at a working distance of 6.5 mm to optimise for both image intensity and spatial resolution for features > 200 nm diameter (maximum size range of $M_{23}C_6$ carbides [20]). Fractography was performed with a secondary electron detector at working distance 10 mm.

Electron backscattered diffraction (EBSD) was performed using an Oxford Instruments symmetry detector at 20 kV and 10 nA at a working distance of 8.5 mm, resulting in pattern Hough indexing in Aztec at 1200 Hz. A system magnification of 1000× and a step size of 280 nm was used across a region of 290 μm by 220 μm for each region of interest. Euler data was post-processed in Channel5's HKL software suite for analysis of pole figures, inverse pole figures and local misorientation. Pole figures were calculated in HKL's Mambo using contours with a half width of 10° and data clustering of 5°. For real-space mapping, the data were cleaned to remove wid spikes and fill immediate neighbours with interpolated orientations to between 2-5% of data points. The inverse pole figures were calculated in HKL's Tango and projected from the loading direction (the horizontal direction in the maps shown here). Grains were defined as neighbouring pixels with a misorientation exceeding

10°. Sub-grain misorientation was calculated in Tango using the grain reference orientation distribution function within HKL, which takes the mean grain orientation as the reference orientation and calculates the pixel misorientation relative to the reference for all pixels in the grain.

3 Results

3.1 Mechanical performance

Prior to heat treatment, the presence of the weld has a drastic effect on the deformation patterning by increasing strain localisation and heterogeneity during tensile deformation. We show this in Figure 3 with the ε_{22} data for the full-field DIC strain maps for each condition at 25, 50, 75 and 100% time to fracture. The specimens with and without a weld show very different behaviour; the latter shows diffuse necking followed by high strain concentration at the neck, plastic instability and fracture, whereas the presence of the weld induces regions of high shear either side of the central, harder weld region. The effect of the heat treatment is different for the specimens with and without a weld. Where there is no weld present after HT, the strain heterogeneity due to the neck occurs at a shorter fraction of lifetime in comparison to the base material with no heat treatment, i.e. there is less evidence for a diffuse necking phase and strain localisation occurs more quickly. Where there is a weld present after HT, there is some early shear banding in the post-weld heat treatment (PWHT) welded region. This banding is highlighted in the figure by arrows and becomes clear at 50% and 75% time to failure. This shear banding region competes with the high strain localisation in the diffuse neck prior to fracture. Importantly, the deformation maps in Figure 3 part d) show that after heat treatment the tensile properties in the weld region are different to the non-welded regions either side of the weld.

A more immediate and direct way to assess the effectiveness of PWHTs towards performance homogeneity is with hardness measurements, which we show in Figure 4 with the hardness maps for the LW pre- and post-HT. Note that the black dots are the points at which data was collected and the values have been interpolated between these points. There is a missing data point in the specimen prior to heat treatment (grey area in the central weld region), which is where data was removed due to being exceptionally soft, likely because of a sub-surface void. Prior to PWHT the weld is harder than the base material by a factor of approximately 1.8. After PWHT there is homogeneity across the base material and the weld region with approximately the same hardness of the base material prior to PWHT. Before PWHT, the weld shows higher hardness lobes either side of the centre line.

The hard region in the as-welded condition shown in Figure 4 is approximately 6 mm-wide. The strain maps in Figure 3 part b) show that the central region in the as-welded specimen experiences only elastic deformation under tension to failure and this region is also 6 mm-wide. We can therefore conclude that the plastic deformation appears to be fully contained within the base material next to the weld and does not occur in the weld region nor in any neighbouring heat affected zone. Interestingly, the region with the highest strain in Figure 3 part b) is not immediately adjacent to the hard weld region but at a distance approximately 1.5 mm from it. This length scale is half the original width of the specimen and therefore is dependent on the specimen geometry. We therefore propose that the region immediately next to the hard weld region is constrained by the hard region and the specimen geometry such that its plastic deformation is limited.

To compare the strain data to that which would be obtained by a physical extensometer, we have used the virtual extensometer method (strain method 1) with a length of 20 mm to obtain engineering stress-strain data to failure for each of the four specimens. We show the results of this

approach in Figure 5. If we compare the specimens with and without a weld prior to the HT, we observe that the presence of the weld slightly decreases tensile strength, increases the strain hardening and it significantly decreases both the strain at ultimate tensile strength (UTS) and total strain at failure. As we conclude that all of the plasticity occurs in the base material for these specimens, similarity in yield and UTS is expected [15,18].

The PWHT affects the stress-strain curves for the specimens with and without a weld differently, just as we observed for the full-field maps in Figure 3. The virtual extensometry shows that the PWHT decreases the yield stress and tensile strength of the welded material but does not affect the elongation associated with the tensile strength nor fracture as compared to the AR condition. The base material with no weld experiences a similar reduction in yield stress and tensile strength, but the strain at tensile strength and at fracture is significantly reduced. In both cases for the HT specimens, we observe in Figure 3 that fracture occurs in the base material. However, in the LW material we observe that there is deformation in the weld region in addition to the neck; these regions compete and create a greater elongation to tensile strength and fracture. These observations point towards microstructural differences between the weld region and the base material, even after PWHT and even though the hardness is homogeneous. To investigate this further, we have calculated the strain heterogeneity as the pixel strain divided by the average strain for the maximum shear strain component,

$$Norm.\,\varepsilon_{MS} = \frac{\varepsilon_{MS}}{\overline{\varepsilon_{MS}}} \tag{5}$$

By plotting normalised frequency of Norm. ε_{MS} on a log-log scale for each of the specimens in Figure 6, we can define greater strain heterogeneity as an extended tail in the of Norm. ε_{MS} distribution. As expected, the amount of strain heterogeneity increases with time. To quantify this heterogeneity, we have calculated the gradient of the high end tails (m_{MS}) as a function of time and we plot this in Figure 7 part a). If we define $m_{MS} < -5$ as homogeneous strain then we can quantify the proportion of time that a specimen spends in a state of homogeneous deformation. We show the results of this approach in Figure 7 part b). This is a quantified value of deformation homogeneity which confirms what we observe in the full-field data in Figure 3 and in the virtual extensometer stress-strain data in Figure 5; the base material that has experienced the HT is heterogeneous earliest, whereas the LW material with the same HT undergoes homogeneous deformation for longer.

We have extracted strain data from the full-field maps using the region of interest method (strain method 2) to compare the strain evolution at the location of fracture. This approach limits the influence of the geometry on the strain data, i.e. the size and shape of the specimen relative to the size of the weld and the length of the extensometer chosen. This was performed with a pixel size in the tensile direction of 0.28 mm and the strain values were averaged over the width of the specimen. We show the results of this approach in Figure 8, which highlights several interesting aspects that are not found in the virtual extensometer method. Firstly, the total strain at failure for the fracture position is similarly large for all specimens. This is very different to the case described by the virtual extensometer in Figure 5, for which strain values will vary depending on the specimen geometry, the extensometer size and the size of any influencing inclusions, such as the hard weld region. Secondly, we can use the stress-strain data at the point of fracture to infer something about strain hardening; the base material strain hardens more in the absence of a weld, both pre- and post-HT. This is interesting because it suggests that the mechanisms of local strain hardening can be affected by competing mechanisms of deformation when a weld or difference in microstructure is

present elsewhere, a hypothesis supported by the full-field measurements in Figure 3 and the strain heterogeneity gradient analysis in Figure 7. Thirdly, the strain-softening post-necking occurs at a similar rate with respect to strain at the fracture point for all specimens, suggesting similar mechanisms of damage accumulation towards failure.

3.2 Characterisation

The strain at the fracture position is similar for all of the specimens but the stresses are different when comparing the pre- and post-HT specimens. Although the strain-softening rates are similar for all specimens, we suggest the absolute differences in stress affect failure. Specifically, high stresses will cause more sudden onset of crack propagation at failure. In support of this hypothesis we observe similar fractography in the specimens with and without a weld, showing similar features that are dissimilar to the fractography in the heat treated specimens with and without a weld. The images in Figure 9 show that for the material that is not heat treated the fracture surface is characterised by sharp, angular features and cracks at ± 45 ° to the loading axis, suggesting sudden crack propagation and brittle fracture. In contrast, the fracture surfaces for the heat-treated specimens are smoother. We suggest that this difference is due to the higher stresses in the non-heat-treated specimens and a resulting sudden failure event. Conversely, in the heat-treated specimens there are larger grains that allow for more shape change and plasticity before fracture.

Backscattered electron imaging has been performed in the SEM to investigate the likely causes for the increased hardness of the weld and how this compares after the heat treatment. Figure 10 shows the microstructure for the as-welded material. There are spheroidal secondary phases with diameters approximately 200 nm decorating the lath boundaries in the BM, consistent with $M_{23}C_6$ carbides [28]. There are also smaller spheroidal particles within the laths approximately 50 nm in diameter, possibly consistent with MX carbides but pushing the spatial resolution of the LaB_6 electron gun. In the HAZ of the as-welded material there are very few carbides and the lath morphology is much finer, accounting for the high hardness in this region by a Hall-Petch type relationship. In the FZ of the as-welded material the grains are large and have a strong lath morphology. While there is some evidence in Figure 10 part l) of small carbides within the laths in the FZ of diameters < 50 nm, this is too close to the spatial resolution of the LaB6 electron gun to report with any certainty. There are no spheroidal carbides on lath boundaries observed in the FZ, suggesting that the carbon is completely dissolved in solution within a fully martensitic microstructure, increasing the hardness relative to the BM but not relative to the fine-lath structure in the HAZ. Figure 11 shows the microstructure for the welded material after the PWHT. After the heat treatment there are carbides present in the base material, the HAZ and the FZ but with a significantly lower density in the FZ. The lath size after the heat treatment are comparable in all three areas. Therefore, we can conclude that the heat treatment was performed successfully regarding homogeneity in lath size and carbide precipitation, i.e. that tempered martensite is formed. However, the carbide size, morphology, density and location are not as well-defined as they are in the as-received material.

To investigate the effect of texture on strain heterogeneity and mechanical performance, we have performed EBSD texture scans and calculated pole figures for the {100}, {110} and {111} planes, shown in Figure 12. The base material (BM) in the AW condition shows a classic rolling texture [29] but is rather weak. This texture deviates in the fusion zone (FZ) and heat-affected zones (HAZ), where the distribution of orientations is more heterogeneous and there are greater intensity peaks due to larger grains, resulting in stronger local texture. After heat treatment the BM shows some

resemblance to the original BM but there is more randomness in the off-peak positions and the peaks themselves are stronger, again due to increased grain size. The patterning in the pole figures of the BM post-HT are not repeated in the FZ nor in the HAZ.

Performance is also affected by the prior austenite grain size and stored energy in the form of dislocation density. To investigate the effect that the HT has on these properties, we show characteristic inverse pole figures (from the loading direction) and grain reference orientation deviation (GROD) maps in Figure 13 and we show the corresponding distribution of grain sizes and misorientation in Figure 14. In the BM prior to any heat treatment the Eurofer-97 grains are equiaxed and have diameters of approx. 5 μm (mode) or approx. 10 μm (mean), as expected [30,31]. After the heat treatment the grain size distribution tails are wider because there are many more larger diameter grains in the base material and even larger grains in the fusion zone. The misorientation maps and distributions show that after the heat treatment there is greater misorientation in all areas of interest and especially in the fusion zone, which is indicative of greater dislocation density and greater stored energy [32–34]. Therefore, the heat treatment has been successful in producing the correct lath size and phase composition through carbide precipitation, but the historical presence of the weld remains visible in the grain size and the orientation distribution.

If the heat treatment had truly homogenised the microstructure, as the hardness maps suggest, then we might expect the grain size, carbide density, texture and ultimately mechanical behaviour to be the same in the base material and fusion zone following the heat treatment. We have shown that this is not the case, and, although we can achieve hardness homogeneity with a given heat treatment, the microstructure remains different between the welded and non-welded regions in terms of grain size and morphology, carbide density, texture and stored energy.

When there is large strain heterogeneity in the as-welded condition, traditional clip-on extensometry averages the measurement of strain, which is not suitable because it ignores the size of the heterogeneity relative to the specimen geometry and it ignores the extent of the heterogeneity in comparison to the extensometer length over which the data is averaged. The use of such an extensometer makes such results difficult to interpret, which we highlight by comparing the two methods of measuring strain in Figure 5 and Figure 8. For highly heterogeneous systems such as a weld, macroscopic differences in properties causes strain localisation in the softer material that can compete with other locations at symmetrical positions in the gauge length to increase the overall elongation. Therefore, specimen geometry plays a significant role in quantifying weld performance. Furthermore, microstructural differences allow strain localisation to evolve at competing sites, increasing overall elongation. We can quantify and isolate these mechanisms of plastic evolution through full-field techniques, which are essential to explain local damage mechanisms in the vicinity of macroscopic and microstructural heterogeneity.

4 Discussion

In comparing the material before heat treatment both with and without a weld, the average stress-strain data in Figure 5 shows that the strain at UTS is lower in the specimen with a weld, which is consistent with lower elongation at UTS for welds in mild steel [18] and lower ductility in TIG welded F82H [15]. The virtual extensometry takes the deformation of the whole specimen into consideration and so the UTS occurs at lower average strain because there is physically less material experiencing plasticity. Interestingly, ductility is not much reduced in electron beam welded F82H

[15], likely because of the slim volume of material in the fusion zone. Conversely, the fracture point stress-strain data in Figure 8 shows that, prior to the heat treatment, the strain at UTS is greater for the specimen with a weld (0.12) than without a weld (0.07). This is important because traditional extensometry implies that the deformation incurred at maximum strength is reduced due to the weld, often explained in terms of triaxiality and promoted cavity development [15,35,36]. As the strain at the point of fracture is a local measurement, our result implies that more deformation is allowed to accumulate at the maximum strength because of the constraint imposed by the hard weld region, the high degree of strain localisation it induces and the competing necking site on the other side of the weld.

As we show in the full-field data, high "X"-shaped strain patterns are generated either side of the weld that suggests that the weld acts as a stress concentrator and possibly introduces stress triaxiality. To our understanding, such patterning has not been observed previously in similar DIC experiments in welds [16,18,19], likely due to lower density speckle patterns and so poorer spatial resolution than the data presented here. Good speckle patterns are essential for high quality full-field data and this is explored in terms of Shannon entropy in section 2.2 of this work. In Figure 3 we show the "X"-shaped patterns as the ε_{22} component because this component has the largest magnitude and is therefore the clearest. However, in reality the deformation is a shear strain, more easily conceptualised as a rotation that accumulates early in the welded specimen like a hard particle rotating in a soft matrix due to strain localisation in the latter [37–39]. We show this explicitly in Figure 15, in which we plot the approximate instance at which the in-plane rotation (ω_3) becomes localised for each of the four specimens, using red as a clockwise rotation and blue as anti-clockwise. For the as-welded specimen the rotation occurs early, just after yield. In contrast, for all of the other specimens the localised rotation occurs later to accompany necking, either just before or just after the ultimate tensile strength is reached. In the as-welded specimen, the reduced elongation to fracture is explained by this early onset of rotation that is usually associated with necking.

The higher hardness in a steel autogenous weld is well known and thought to be due to the as-solidified microstructure being fully martensitic and containing much carbon in solution, which is supported by the backscattered electron images presented here. However, it should be noted that the higher hardness in the weld region has been attributed to a greater density of small MX carbides [40], and although the BSE images shown here might hint at small particles < 50 nm within laths in the FZ, this is pushing the spatial resolution of the analyses here. The hardness profile in the as-welded region has a classic "M"-shape [17], reminiscent of residual stress profiles of a similar shape [9,41,42]. However, this shape could equally be due to microstructural variations, especially as much of the residual stresses will be relieved through specimen preparation. Indeed, here we demonstrate that there are smaller laths in the HAZ compared to both the BM and the FZ, which are a response to higher cooling rates away from the central welding line [11] that increase local resistance to deformation by providing a greater number of boundaries to dislocation motion in a Hall-Petch type relationship [43]. After the normalising and tempering heat treatment the hardness is uniform across the weld region, which is an observation widely supported in the community [44,45] and the motivation for this work. However, we have demonstrated that this homogeneity in hardness does not correspond to homogeneity in microstructure nor behaviour under tension. While possible $M_{23}C_6$ carbides on lath boundaries are found in the FZ after heat treatment as expected [8,46], we have shown that they are not well distributed at boundaries and that the prior austenite grain morphology, texture and stored energy vary across the gauge length. This is likely because the FZ of the AW material does not contain sufficient stored energy to drive grain refinement and the

crystallographic orientations of the FZ limit the possible transformations during heat treatment, directly influencing the final texture after cooling.

After the heat treatment, the average stress-strain data in Figure 5 shows that the strain at UTS is greater in the specimen with a weld. This is largely due to the average measurement of strain including the weld, which deforms significantly even though it is not the point of fracture. This competition is in plastic deformation but not necking, which is why the fracture point stress-strain information shows less strain accumulation in the fracture region at failure. The lath sizes across the gauge length are comparable but the grains in which the laths are contained are larger in the fusion zone, which might suggest that the fusion zone should be softer than the base material [43]. However, it should be noted that the laths are densely packed and so their true size variation will have a greater influence on strength than the size of their bounding prior austenite grains. In contrast, the fusion zone grains show fewer carbides on lath boundaries and have more sub-grain distortions, both of which would suggest that the fusion zone should be harder than the base material [47,48]. We know that the hardness is homogenous across the gauge length so these effects must balance one another. However, in tension this is not the case and we see significant plasticity in the weld region after heat treatment. While this could be due to the larger prior austenite grain size that we show here, it could also be due to a sub-surface pore in the weld region. Indeed, the strain pattern in the weld region of the heat-treated sample show long strands of alternate clockwise and anti-clockwise rotation in the ω_3 component in Figure 15 (specimen LW HT), which is reminiscent of strain patterns that surround a hole [49]. The work presented here would therefore be improved by non-destructive testing to measure pore density in the weld and by repeat testing to assess the consistency in observations. However, our aim here was not to provide a statistical analysis of behaviour but to demonstrate the benefit of using full-field techniques for analysis of deformation phenomena in heterogeneous systems such as these. It is the surface measurement of deformation we use that leads to an uncertainty in the through-thickness deformation homogeneity.

In this work we have introduced the idea of the strain homogeneity distribution gradient in Figure 6 and Figure 7, which is an adaptation of a similar approach in high-resolution DIC in a two-phase Ti alloy [50]. This is a way of highlighting the degree to which the whole field of view deviates from the mean strain. We do this because strain heterogeneity often precedes failure in plastic materials [1,2], and so a system that deforms heterogeneously early on is a good indicator of that system's propensity for early failure. We show here that whilst the normalisation and tempering heat treatment performed ensures hardness homogeneity, it creates a situation in which the material deforms heterogeneously, even in the absence of a weld. Therefore, better heat treatments towards weld performance optimisation would be found in a one- or multi-step tempering treatment below the austenitisation temperature in line with recommendations for the ITER blanket component [11]. Alternatively, a less severe normalising stage might be appropriate, as explored for grade 91 steel [46], or a localised tempering treatment at the weld zone to limit over-tempering in the base material.

5 Conclusions

We have presented detailed analyses of the full-field strain evolution of welded Eurofer97 components both with and without a post-weld heat treatment. Our spatial resolution is much improved over previous attempts in the literature and so we are able to understand mechanical properties both globally and locally in terms of both the underlying microstructure and the

rotational strain fields that develop to precede failure. In particular, we can conclude that while the normalising and tempering heat treatment homogenises the hardness across the weld region it does not homogenise the microstructure in terms of carbide size, morphology and location relative to the lath boundary. Further, it does not homogenise the prior austenite grain size, texture, or the sub-grain misorientation, implying heterogeneity in dislocation density and stored energy. Furthermore, the full-field approach to deformation quantification allows us to determine the strain homogeneity distribution gradient, which is a direct measure of the strain localisation that precedes failure and if applied in-situ would provide an indication of early failure. In this approach we have shown that the microstructure produced by the normalisation and tempering heat treatment induces early strain heterogeneity even in the absence of a weld and it is therefore advised that such a heat treatment is avoided in certain engineering applications where even slight volumetric change needs to be avoided due to constraint. Full-field techniques are a useful tool in determining the mechanisms for changes in component performance due any type of heterogeneity. In the case of welds, the suitability of a given PWHT can be understood in terms of spatially-resolved mechanical deformation, which allows us to probe the mechanisms responsible for the macroscopic behaviour we observe.

6 Acknowledgements

The authors would like to acknowledge EPSRC grant EP/T012250/1 and to thank Michael Reith at Karlsruhe Institute for Technology for providing the Eurofer-97 plates for this study.

7 References

[1] T. Pardoen, Y. Brechet, Influence of microstructure-driven strain localization on the ductile fracture of metallic alloys, Philos. Mag. 84 (2004) 269–297. doi:10.1080/14786430310001610366.

[2] N. Bordignon, A. Piccolroaz, F. Dal Corso, D. Bigoni, Strain localization and shear band propagation in ductile materials, Front. Mater. 2 (2015) 1–13. doi:10.3389/fmats.2015.00022.

[3] R.L. Klueh, Elevated temperature ferritic and martensitic steels and their application to future nuclear reactors, Int. Mater. Rev. 50 (2005) 287–310. doi:10.1179/174328005x41140.

[4] J.A. Francis, W. Mazur, H.K.D.H. Bhadeshia, Review Type IV cracking in ferritic power plant steels, Mater. Sci. Technol. 22 (2006) 1387–1395. doi:10.1179/174328406x148778.

[5] D.J. Abson, J.S. Rothwell, Review of type IV cracking of weldments in 9–12%Cr creep strength enhanced ferritic steels, Int. Mater. Rev. 58 (2013) 437–473. doi:10.1179/1743280412y.0000000016.

[6] C. Pandey, M. Mohan, P. Kumar, N. Saini, Some studies on P91 steel and their weldments, J. Alloys Compd. 743 (2018) 332–364. doi:10.1016/j.jallcom.2018.01.120.

[7] R. Lindau, A. Möslang, M. Rieth, M. Klimiankou, E. Materna-Morris, A. Alamo, A.A.F. Tavassoli, C. Cayron, A.M. Lancha, P. Fernandez, N. Baluc, R. Schäublin, E. Diegele, G. Filacchioni, J.W. Rensman, B. V.D. Schaaf, E. Lucon, W. Dietz, Present development status of EUROFER and ODS-EUROFER for application in blanket concepts, Fusion Eng. Des. 75–79 (2005) 989–996. doi:10.1016/j.fusengdes.2005.06.186.

[8] S. Paddea, J.A. Francis, A.M. Paradowska, P.J. Bouchard, I.A. Shibli, Residual stress

distributions in a P91 steel-pipe girth weld before and after post weld heat treatment, Mater. Sci. Eng. A. 534 (2012) 663–672. doi:10.1016/j.msea.2011.12.024.

[9] P. Dong, S. Song, J. Zhang, Analysis of residual stress relief mechanisms in post-weld heat treatment, Int. J. Press. Vessel. Pip. 122 (2014) 6–14. doi:10.1016/j.ijpvp.2014.06.002.

[10] C. Pandey, M.M. Mahapatra, P. Kumar, N. Saini, Effect of strain rate and notch geometry on tensile properties and fracture mechanism of creep strength enhanced ferritic P91 steel, J. Nucl. Mater. 498 (2018) 176–186. doi:10.1016/j.jnucmat.2017.10.037.

[11] P. Aubert, F. Tavassoli, M. Rieth, E. Diegele, Y. Poitevin, Low activation steels welding with PWHT and coating for ITER test blanket modules and DEMO, J. Nucl. Mater. 409 (2011) 156–162. doi:10.1016/j.jnucmat.2010.09.009.

[12] C. Pandey, M.M. Mahapatra, P. Kumar, A. Giri, Microstructure characterization and charpy toughness of P91 weldment for as-welded, post-weld heat treatment and normalizing & tempering heat treatment, Met. Mater. Int. 23 (2017) 900–914. doi:10.1007/s12540-017-6850-2.

[13] G. Taniguchi, K. Yamashita, Effects of Post Weld Heat Treatment (PWHT) Temperature on Mechanical Properties of Weld Metals for High-Cr, Kobelco Technol. Rev. (2013) 33–39.

[14] Y. Yamamoto, X. Yu, S. Suresh Babu, Improvement of creep performance of strength enhanced ferritic (CSEF) steel weldments through non-standard heat treatments, in: Proc. ASME Symp. Elev. Temp. Appl. Mater. Foss. Nucl. Petrochemical Ind., 2019.

[15] T. Nakata, H. Tanigawa, Evaluation of local deformation behavior accompanying fatigue damage in F82H welded joint specimens by using digital image correlation, Fusion Eng. Des. 87 (2012) 589–593. doi:10.1016/j.fusengdes.2012.01.048.

[16] Á.J.F. Pérez, C. Sam, F.E. Alcalá, Measuring Strain Concentrations in Welded Junctions using Digital Image Correlation, Young Weld. Prof. Int. Conf. (2014) 17–21.

[17] Y. Peng, C. Wu, J. Gan, J. Dong, Determination of the local constitutive properties of the welded steel joints using digital image correlation method, Constr. Build. Mater. 171 (2018) 485–492. doi:10.1016/j.conbuildmat.2018.03.182.

[18] K.M. Saranath, A. Sharma, M. Ramji, Zone wise local characterization of welds using digital image correlation technique, Opt. Lasers Eng. 63 (2014) 30–42. doi:10.1016/j.optlaseng.2014.06.006.

[19] K.M. Saranath, M. Ramji, Local zone wise elastic and plastic properties of electron beam welded Ti-6Al-4V alloy using digital image correlation technique: A comparative study between uniform stress and virtual fields method, Opt. Lasers Eng. 68 (2015) 222–234. doi:10.1016/j.optlaseng.2015.01.005.

[20] P. Fernández, M. García-Mazarío, A.M. Lancha, J. Lapeña, Grain boundary microchemistry and metallurgical characterization of Eurofer'97 after simulated service conditions, J. Nucl. Mater. 329–333 (2004) 273–277. doi:10.1016/j.jnucmat.2004.04.055.

[21] S. Kirk, W. Suder, K. Keogh, T. Tremethick, A. Loving, Laser welding of fusion relevant steels for the European DEMO, Fusion Eng. Des. 136 (2018) 612–616. doi:10.1016/j.fusengdes.2018.03.039.

[22] X.Y. Liu, R.L. Li, H.W. Zhao, T.H. Cheng, G.J. Cui, Q.C. Tan, G.W. Meng, Quality assessment of speckle patterns for digital image correlation by Shannon entropy, Optik (Stuttg). 126 (2015) 4206–4211. doi:10.1016/j.ijleo.2015.08.034.

[23] R. Bigger, B. Blaysat, C. Boo, M. Grewer, J. Hu, A. Jones, M. Klein, P. Lava, M. Pankow, K. Raghavan, P. Reu, T. Schmidt, T. Siebert, M. Simonsen, A. Trim, D. Turner, A. Vieira, T. Weikert, A Good Practices Guide for Digital Image Correlation, (2018). doi:10.32720/idics/gpg.ed1/print.format.

[24] G. Dieter, Mechanical metallurgy, 1986.

[25] S. van der Walt, S.C. Colbert, G. Varoquax, The NumPy array: A structure for efficient numerical computation, Comput. Sci. Eng. March/Apri (2011) 22–30.

[26] D. Hunter, J., Matplotlib: A 2D Graphics Environment, Comput. Sci. Eng. May/June (2007) 90–95.

[27] A. Harte, H. Dawson, D. Bowden, S. Kirk, M. Gorley, Full field deformation data: Laser welded Eurofer, Zenodo. (2020). https://doi.org/10.5281/zenodo.3696794.

[28] I. Monteiro De Sena Silvares de Carvalho, Steels for nuclear reactors: Eurofer 97, Delft, The Netherlands, 2016. doi:https://doi.org/10.4233/uuid:a3e32a8c-bc0a-497d-9666-15ec44f2e5c2.

[29] U.F. Kocks, C.N. Tome, H.-R. Wenk, Texture and anisotropy: Preferred orientations in polycrystals and their effect on materials properties, Cambridge University Press, 1998.

[30] S. Rieth, M. Schirra, EUROFER 97: Tensile, charpy, creep and struetucral tests, (2003).

[31] L. Pilloni, C. Cristalli, O. Tassa, I. Salvatori, S. Storai, Grain size reduction strategies on Eurofer, Nucl. Mater. Energy. 17 (2018) 129–136. doi:10.1016/j.nme.2018.06.023.

[32] P. Gerber, T. Baudin, S. Jakani, M.H. Mathon, B. Bacroix, Estimation of stored energy distribution from EBSD measurements, Mater. Sci. Forum. 467–470 (2004) 51–56. doi:10.4028/www.scientific.net/msf.467-470.51.

[33] A. Godfrey, O. V. Mishin, T. Yu, Characterization and influence of deformation microstructure heterogeneity on recrystallization, IOP Conf. Ser. Mater. Sci. Eng. 89 (2015). doi:10.1088/1757-899X/89/1/012003.

[34] Y. Takayama, T. Yoshimura, H. Watanabe, Relationship between strain stored by compressive deformation and crystallographic orientation in a pure aluminum, IOP Conf. Ser. Mater. Sci. Eng. 82 (2015). doi:10.1088/1757-899X/82/1/012029.

[35] J.R. Rice, D.M. Tracey, On the ductile enlargement of voids in triaxial stress fields, J. Mech. Phys. Solids. 17 (1969) 201–217.

[36] G. Mirone, Role of stress triaxiality in elastoplastic characterization and ductile failure prediction, Eng. Fract. Mech. 74 (2007) 1203–1221. doi:10.1016/j.engfracmech.2006.08.002.

[37] S. Jammes, L.L. Lavier, J.E. Reber, Localization and delocalization of deformation in a bimineralic material, J. Geophys. Res. Solid Earth. 120 (2015) 3649–3663. doi:10.1002/2015JB011890.

[38] D. Cyprych, S. Brune, S. Piazolo, J. Quinteros, Strain localisation in polycrystalline material with second phase particles: Numerical modelling with application to ice mixtures, Geochemistry Geophys. Geosystems. 17 (2016) 3608–3628. doi:10.1002/2015GC006060.Received.

[39] W. Yang, Q. Liu, Z. Yue, X. Li, B. Xu, Rotation of hard particles in a soft matrix, J. Mech. Phys. Solids. 101 (2017) 285–310. doi:10.1016/j.jmps.2017.01.008.

[40] S. Zhang, T. Melfi, B.K. Narayanan, Effects of precipitates on mechanical properties of P91 submerged arc welds, Sci. Technol. Weld. Join. 21 (2015) 147–156. doi:10.1179/1362171815y.0000000076.

[41] K.A. Venkata, S. Kumar, H.C. Dey, D.J. Smith, P.J. Bouchard, Study on the Effect of Post Weld Heat Treatment Parameters on the Relaxation of Welding Residual Stresses in Electron Beam Welded P91 Steel Plates, Procedia Eng. 86 (2014) 223–233. doi:10.1016/j.proeng.2014.11.032.

[42] H. Dawson, M. Serrano, S. Cater, P. Wady, T. Pirling, E. Jimenez-melero, Residual stress distribution in friction stir welded ODS steel measured by neutron diffraction, J. Mater. Process. Technol. 246 (2017) 305–312. doi:10.1016/j.jmatprotec.2017.03.013.

[43] R.W. Armstrong, Engineering science aspects of the Hall-Petch relation, Acta Mech. 225 (2014) 1013–1028. doi:10.1007/s00707-013-1048-2.

[44] M. Abd El-Rahman Abd El-Salam, I. El-Mahallawi, M.R. El-Koussy, Influence of heat input and post-weld heat treatment on boiler steel P91 (9Cr-1Mo-V-Nb) weld joints: Part 2 - Mechanical properties, Int. Heat Treat. Surf. Eng. 7 (2013) 32–37. doi:10.1179/1749514813Z.00000000051.

[45] V.L. Manugula, K. V. Rajulapati, G.M. Reddy, K.B.S. Rao, Role of evolving microstructure on the mechanical properties of electron beam welded ferritic-martensitic steel in the as-welded and post weld heat-treated states, Mater. Sci. Eng. A. 698 (2017) 36–45. doi:10.1016/j.msea.2017.05.036.

[46] C. Pandey, M.M. Mahapatra, P. Kumar, N. Saini, Homogenization of P91 weldments using varying normalizing and tempering treatment, Mater. Sci. Eng. A. 710 (2018) 86–101. doi:10.1016/j.msea.2017.10.086.

[47] R.R. Shen, V. Ström, P. Efsing, Spatial correlation between local misorientations and nanoindentation hardness in nickel-base alloy 690, Mater. Sci. Eng. A. 674 (2016) 171–177. doi:10.1016/j.msea.2016.07.123.

[48] B. Liu, T. Qin, W. Xu, C. Jia, Q. Wu, M. Chen, Z. Liu, Effect of tempering conditions on secondary hardening of carbides and retained austenite in spray-formed M42 high-speed steel, Materials (Basel). 12 (2019). doi:10.3390/ma12223714.

[49] B. Pan, J. Yuan, Y. Xia, Strain field denoising for digital image correlation using a regularized cost-function, Opt. Lasers Eng. 65 (2015) 9–17. doi:10.1016/j.optlaseng.2014.03.016.

[50] D. Lunt, T. Busolo, X. Xu, J. Quinta da Fonseca, M. Preuss, The effect of nanoscale a2 precipitation on strain localisation in a two-phase Ti-alloys, Acta Mater. 129 (2017) 72–82. doi:10.1016/j.actamat.2016.10.035.

8 Figures

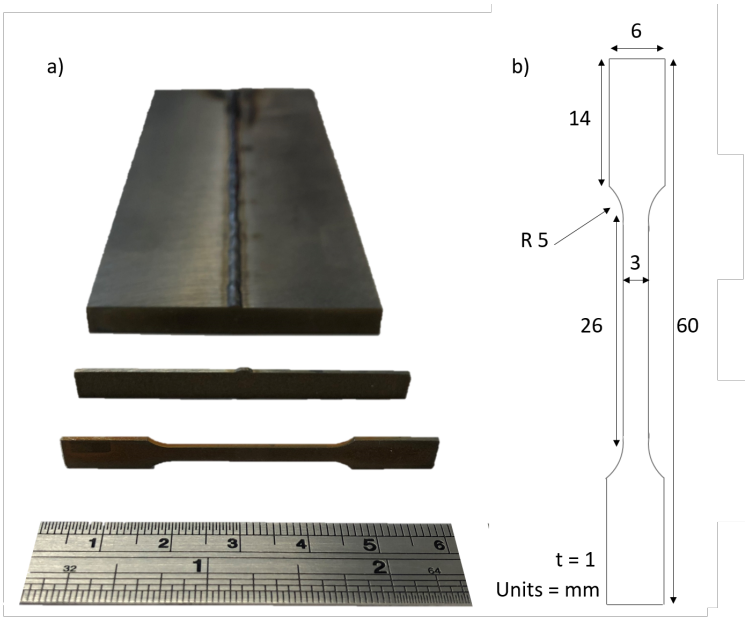

Figure 1 Microtensile specimens taken from the cross section of the weld as shown in part a) and machined by EDM into the geometry shown in part b) with thickness (t) of 1 mm, a chamfer radius (R) of 5 mm for a gauge length of 26 mm and gauge width 3 mm.

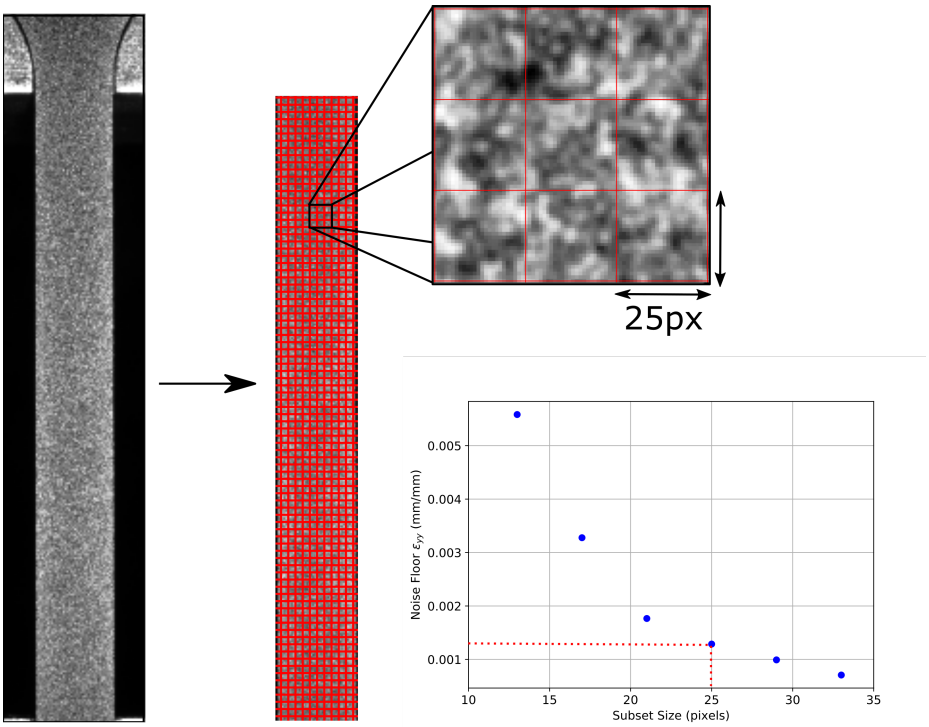

Figure 2 The speckle pattern and pixel subset size selection as a function of the uncertainty, calculated here as the noise floor in the ε_{yy} strain component. For this speckle pattern, a subset size of 25 pixels was found to give a reasonable balance between minimising uncertainty in the measurement of strain (larger subsets) and the best spatial resolution (smaller subsets).

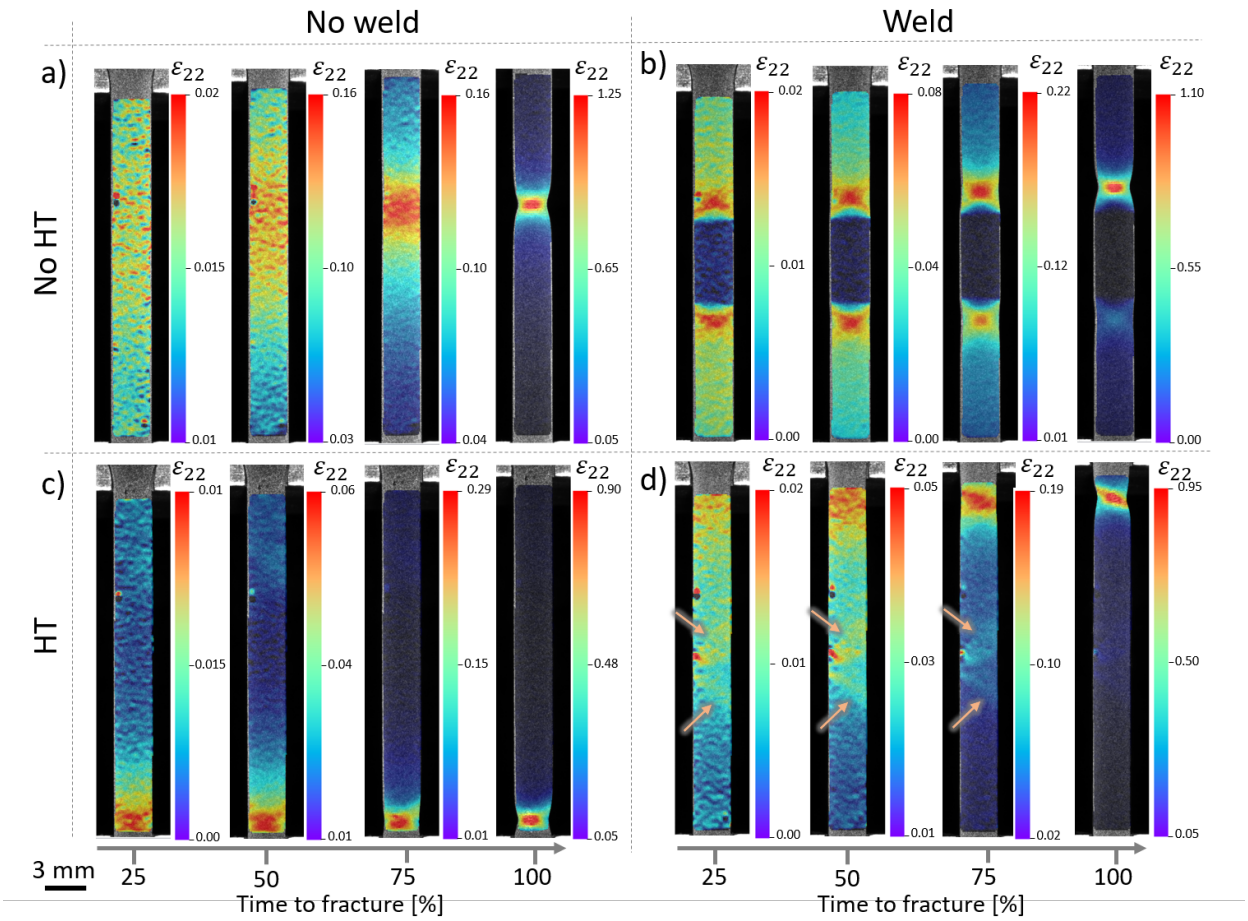

Figure 3 The ε_{22} component maps from full-field DIC at 25, 50, 75 and 100% time to fracture for specimens with and without a weld and with and without the heat treatment (HT). The arrows in part d) point to shear-dominated regions in the weld region that initiate early on during the test.

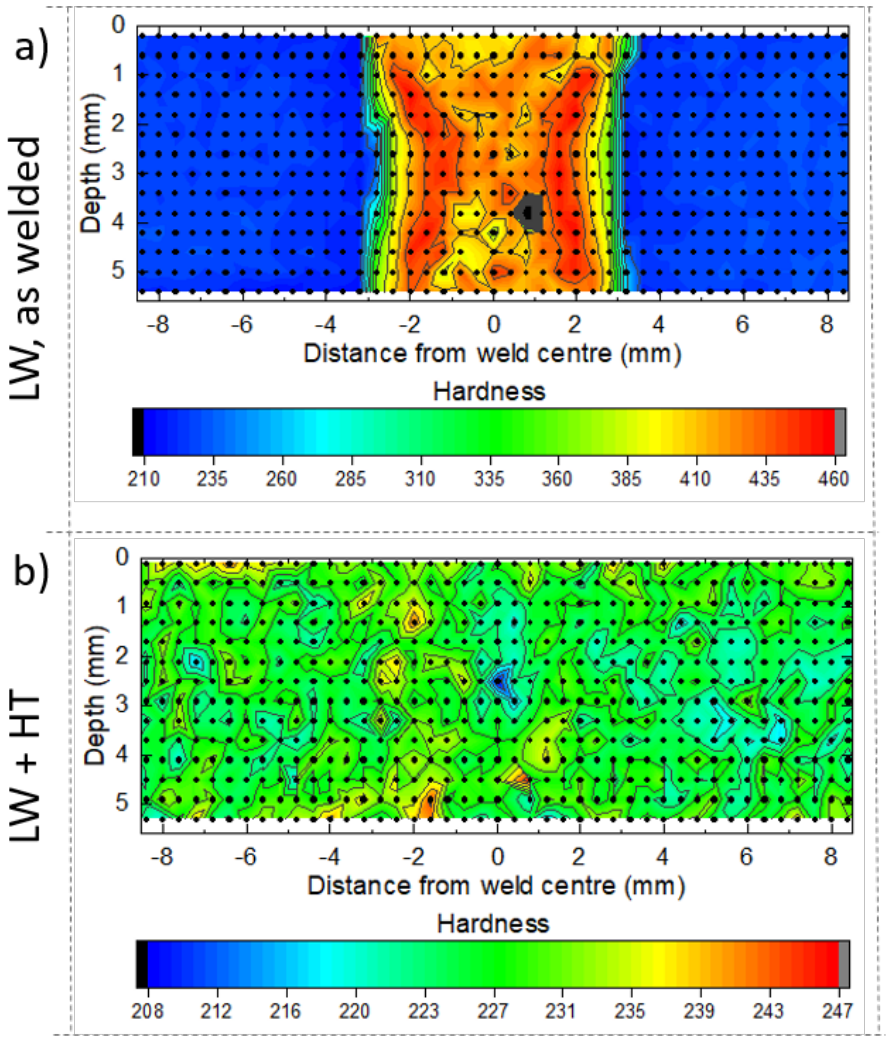

Figure 4 The hardness profiles across the weld region before and after heat treatment (HT).

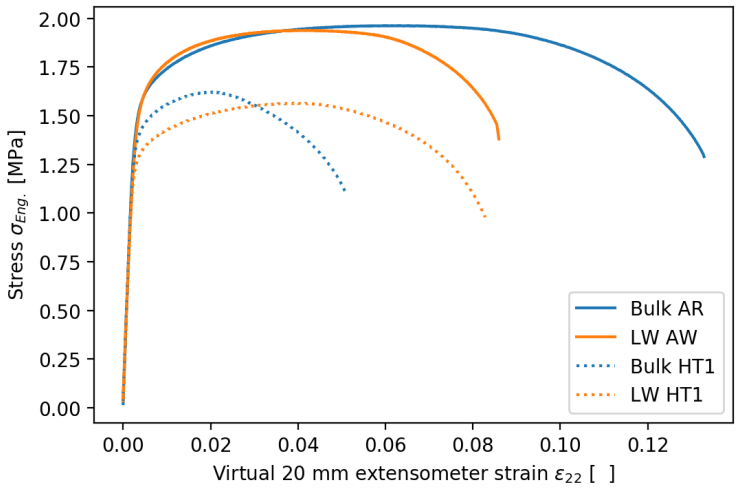

Figure 5 Engineering stress-strain and plots for virtual extensometer of 20 mm gauge length for the bulk as-received (AR) material and the laser welded (LW) material in the as-welded (AW) condition and after the heat treatment (HT).

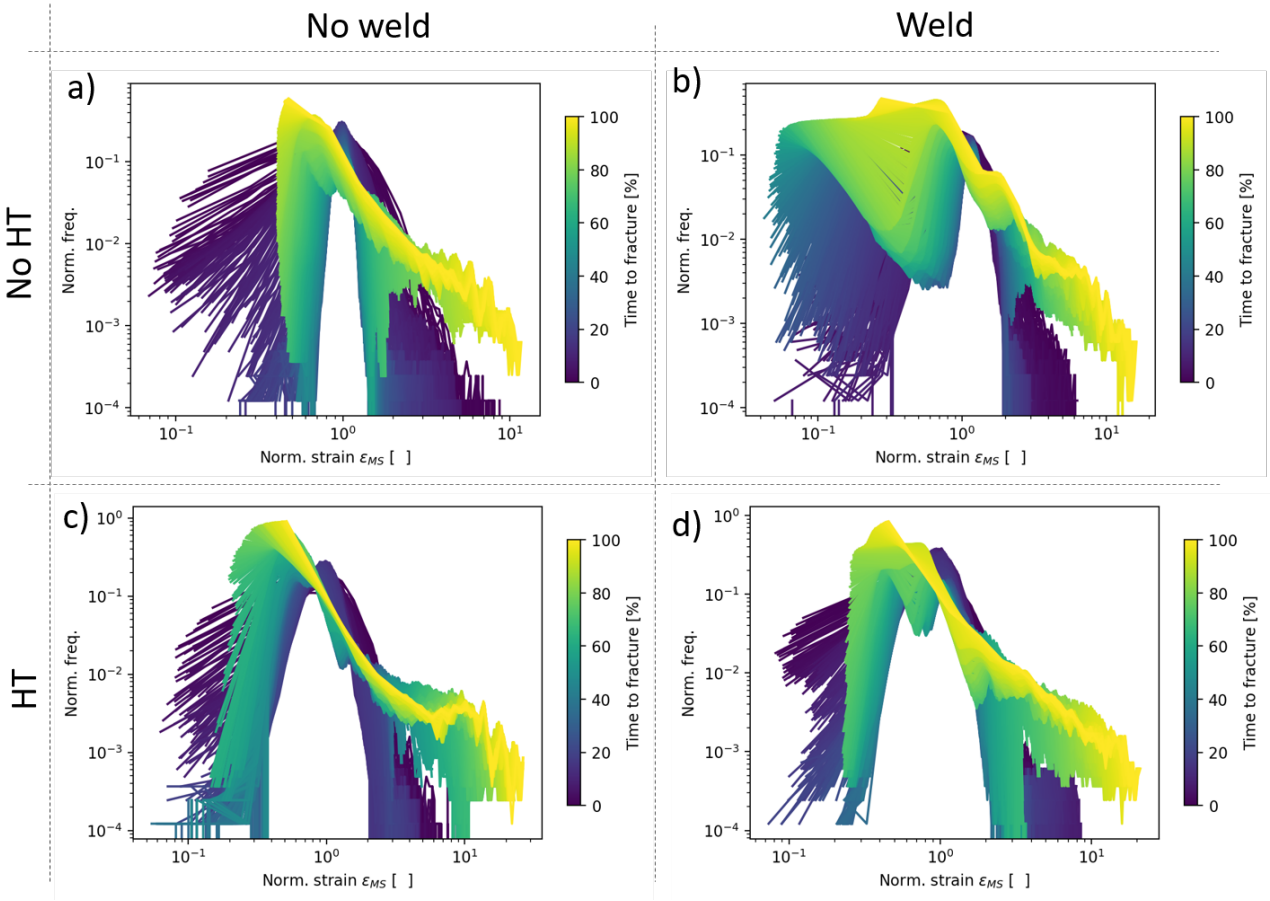

Figure 6 The normalised frequency distributions of normalised maximum shear strain (strain normalised to specimen mean strain) as a function of % time to fracture for the welded and the non-welded specimen both with and without the heat treatment (HT). Wider distributions signify greater deviation from the mean strain and therefore greater strain heterogeneity.

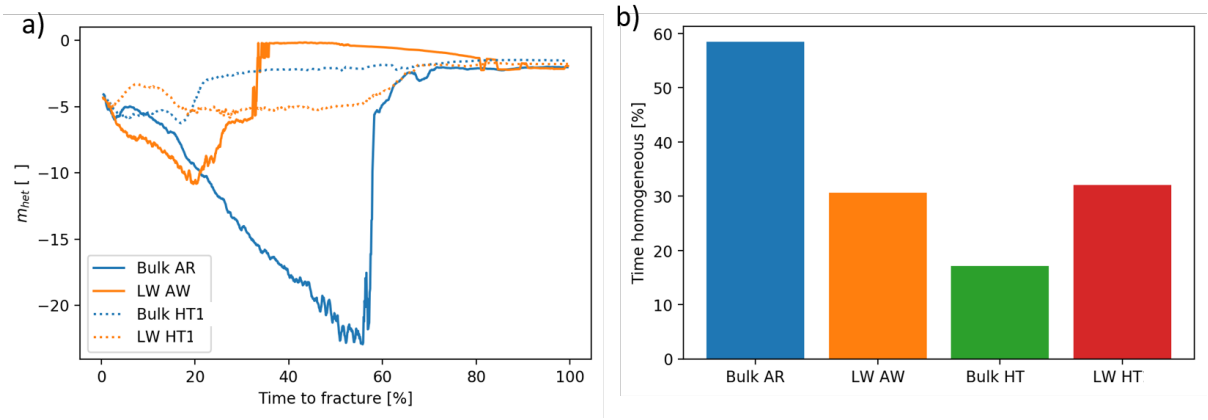

Figure 7 a) The gradient of the log-log histograms in Figure 6 as a function of time and b) the amount of time spent in the homogeneous deformation regime (< -5 m_{het}) for the bulk as-received (AR) material and the laser welded (LW) material in the as-welded (AW) condition and after the heat treatment (HT).

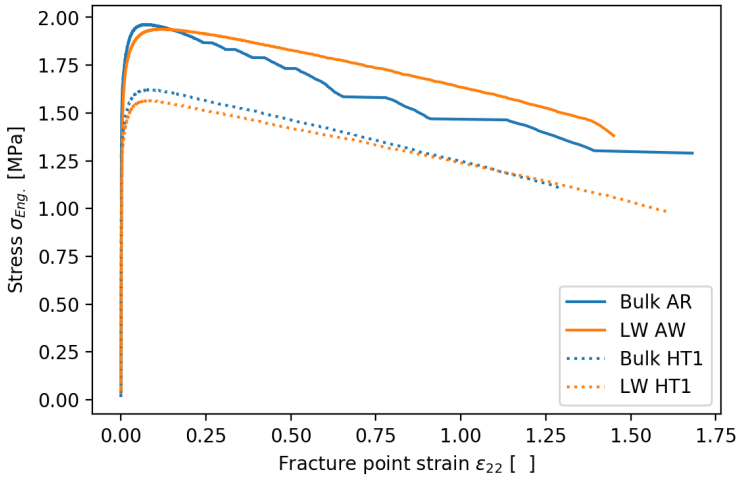

Figure 8 Engineering stress-strain curves derived from averaging the strain over a small region at the point of fracture for the bulk as-received (AR) material and the laser welded (LW) material in the as-welded (AW) condition and after the heat treatment (HT).

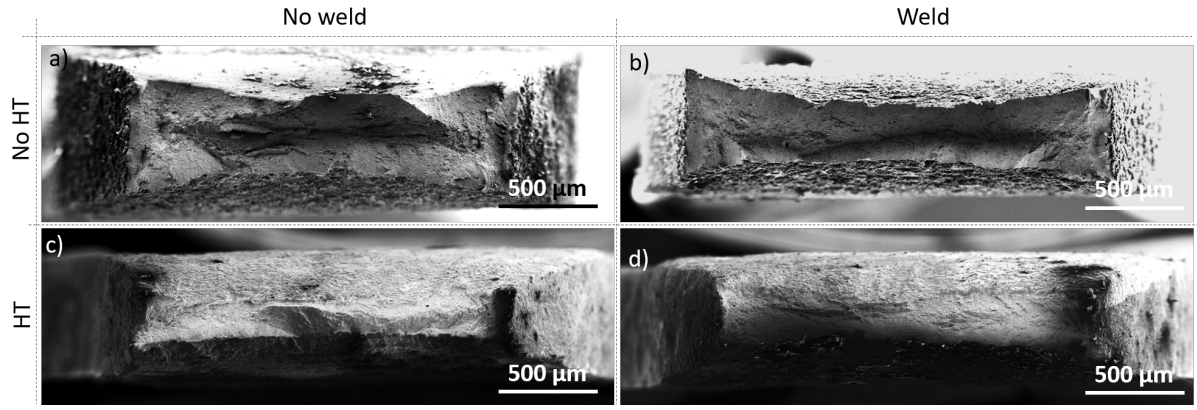

Figure 9 Secondary electron images showing the tensile fracture surfaces after failure for specimens with and without a weld and with and without a heat treatment (HT). The contrast arises from surface topography.

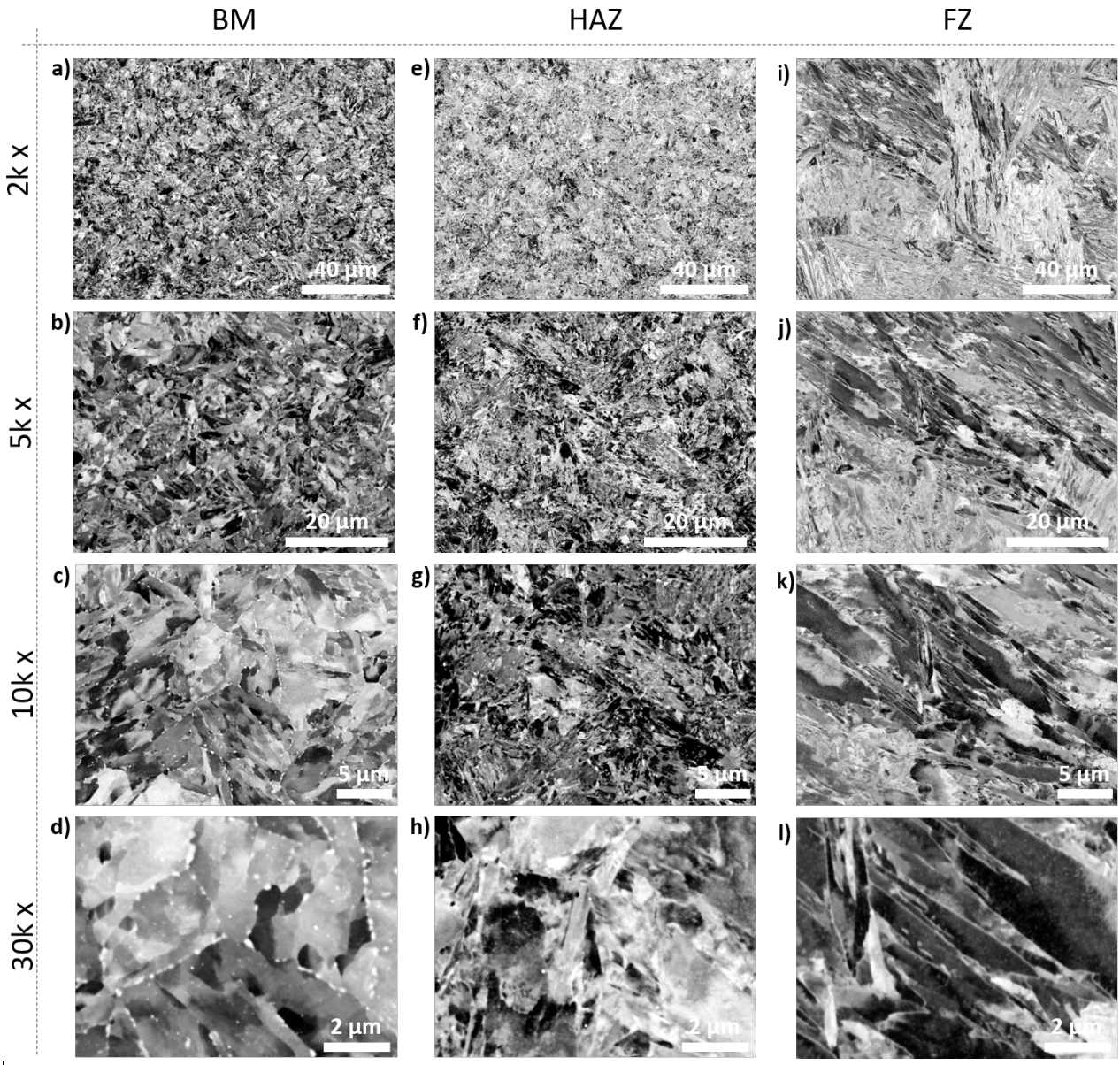

Figure 10 Backscattered electron images of the microstructure in the welded specimen is the as-welded state. Images were taken from the base material (BM), the heat-affect zone (HAZ) and the fusion zone (FZ) at magnifications 2kx, 5kx, 10kx and 30 kx. The contrast arises from crystallographic orientation and phase composition.

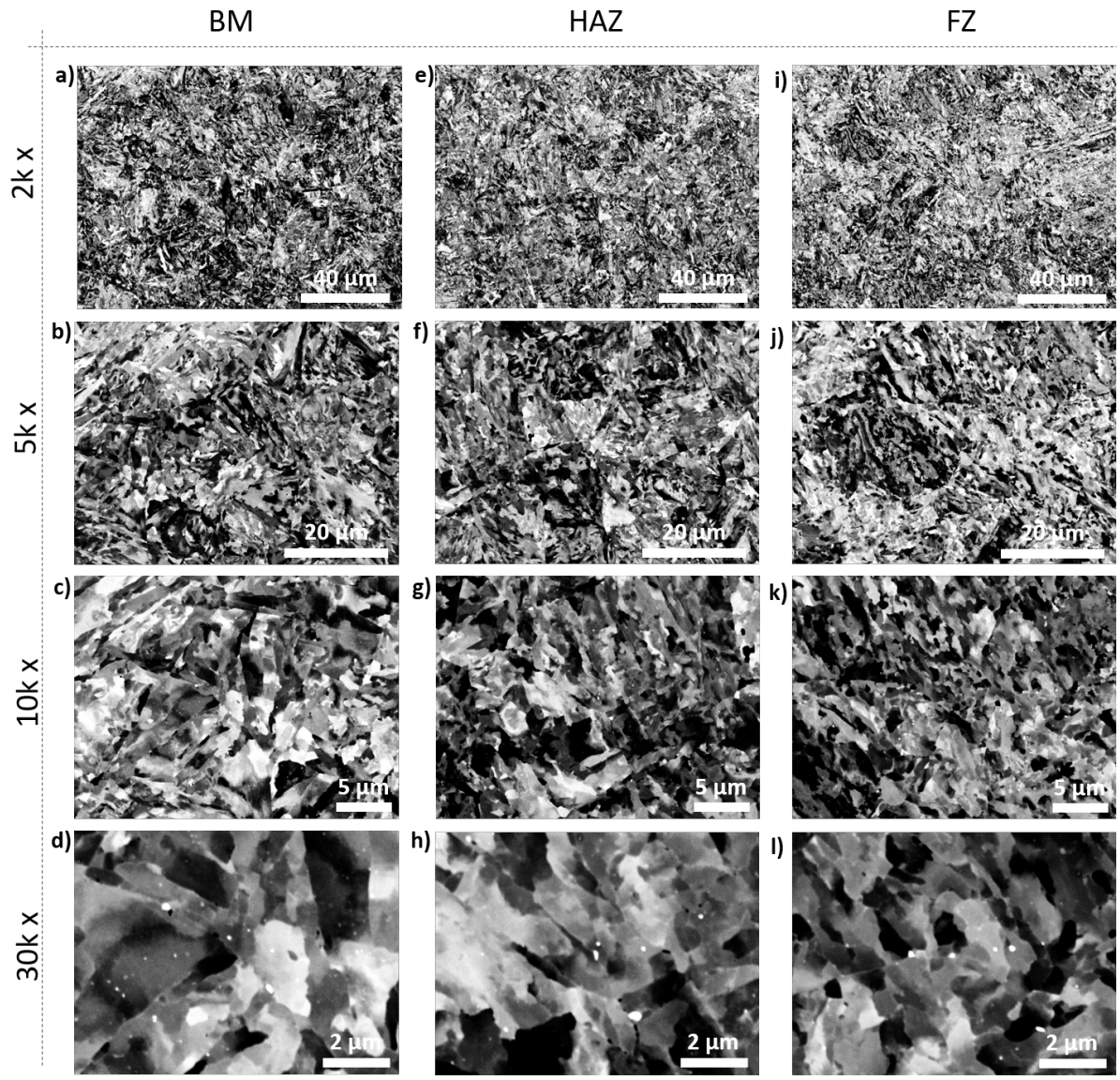

Figure 11 Backscattered electron images of the microstructure in the welded specimen after the post-weld heat treatment. Images were taken from the base material (BM), the heat-affect zone (HAZ) and the fusion zone (FZ) at magnifications 2kx, 5kx, 10kx and 30 kx. The contrast arises from crystallographic orientation and phase composition.

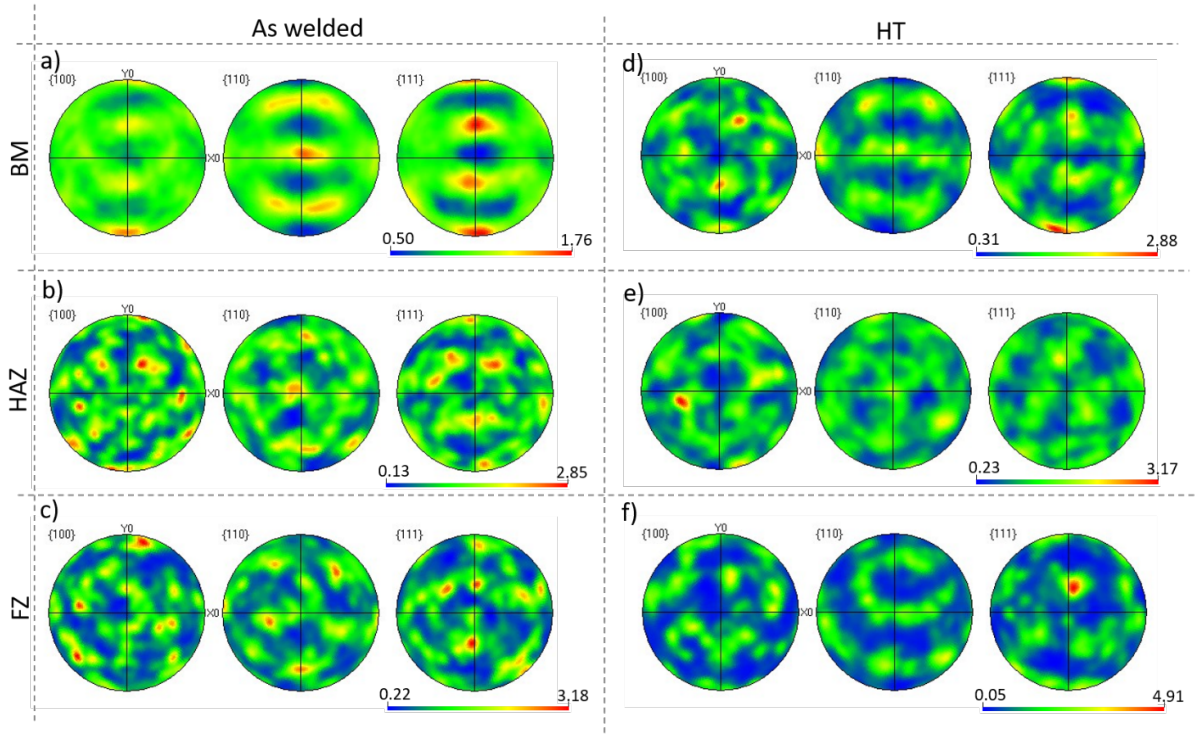

Figure 12 Pole figures for different regions of the welded specimens in the as-welded and heat treated (HT) condition. The regions of interest are the base material (BM), the heat affected zone (HAZ) and the fusion zone (FZ). The colour scale is in multiples of random.

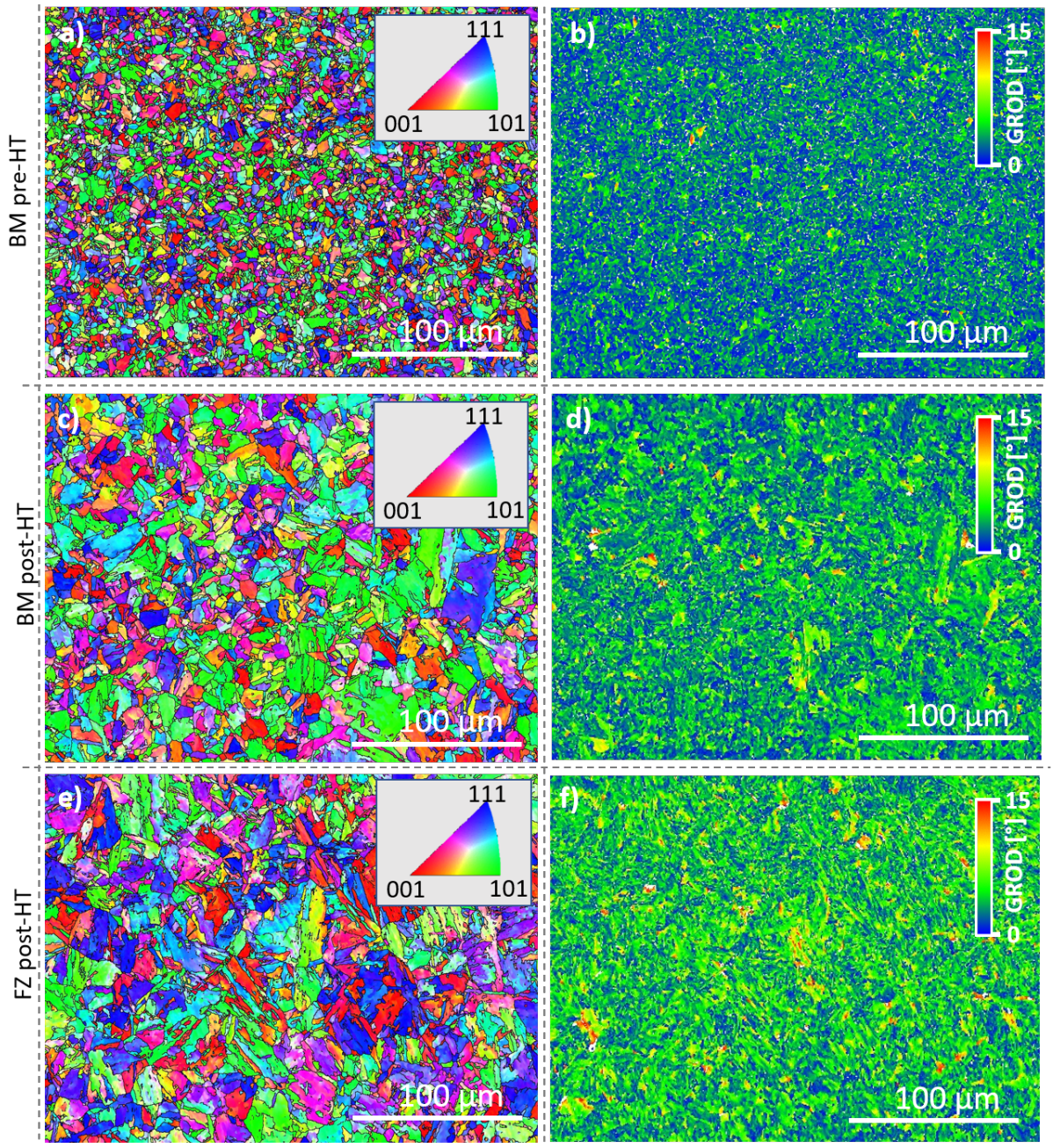

Figure 13 EBSD orientation data presented as IPF maps (left) from the loading direction (horizontal) and misorientation maps (right, misorientation calculated as the grain reference orientation distribution) for different regions of the welded material before and after heat treatment (HT). The regions of interest are the base material (BM) and the fusion zone (FZ).

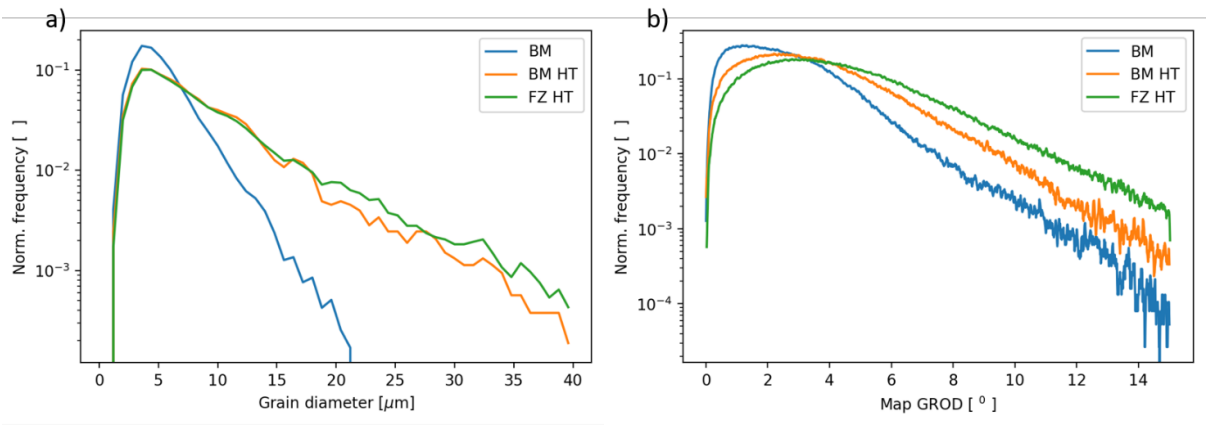

Figure 14 a) Grain diameter and b) misorientation distribution (calculated as the grain reference orientation distribution, GROD) for the three maps in Figure 13. The regions are the base material (BM) in the as-received condition and the fusion zone (FZ) before and after the heat treatment (HT).

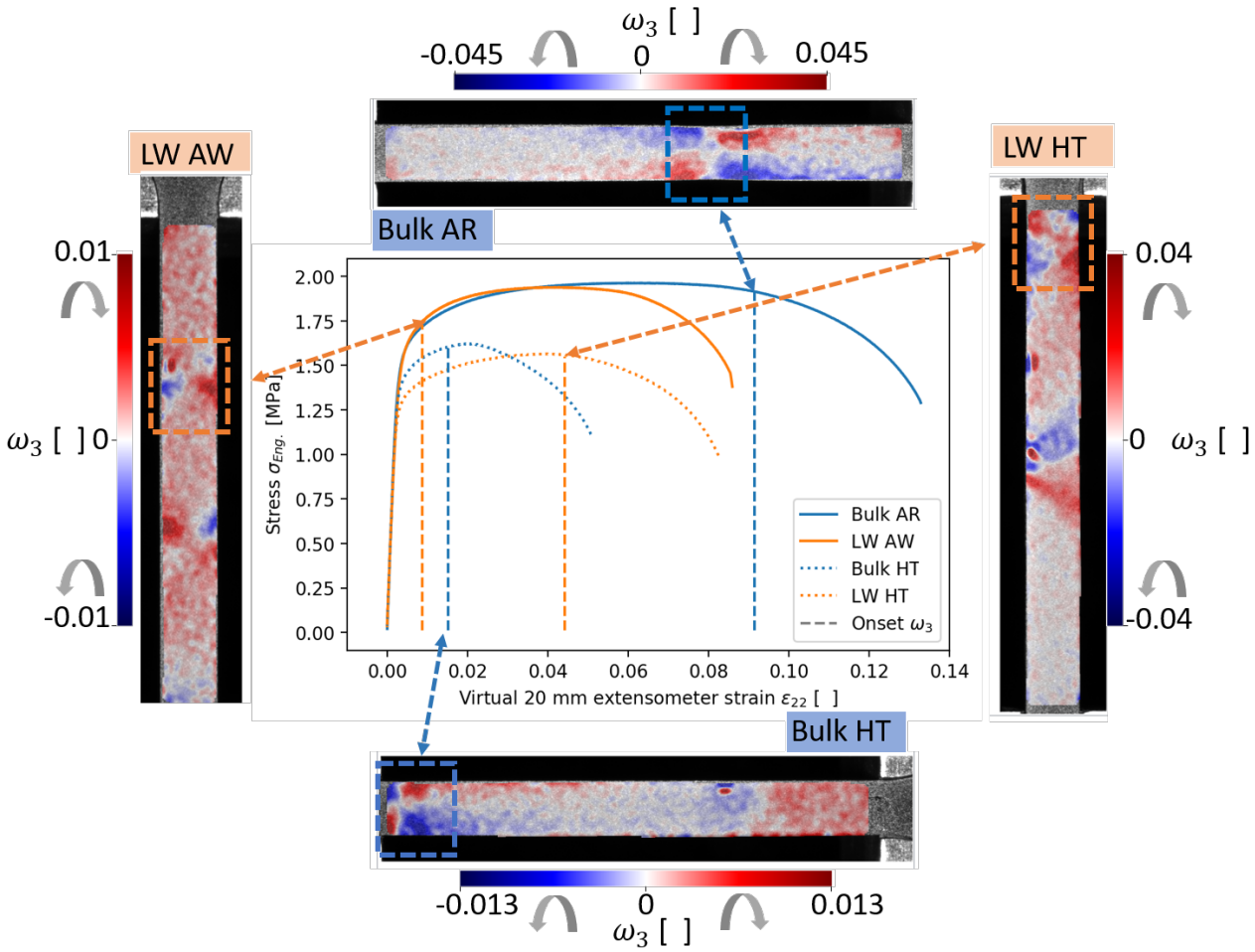

Figure 15 The approximate instances at which the in-plane rotation ω_3 becomes clear in the full-field data for each of the four conditions of the laser weld (LW) and the bulk material in the as-welded (AW) or as-received (AR) state before and after heat treatment (HT). The instant at which ω_3 heterogeneity at the eventual fracture point becomes clear is highlighted with dotted lines on the virtual extensometry engineering stress-strain data, corresponding to the dotted box in the ω_3 maps.

9 Tables

Table 1 - Parameters used to perform DIC in DaVis 10.

Parameter	Value
Method	Sum of difference
Subset size	25 x 25 pixels
Step Size	8 pixels
Cameras	LaVision M-Lite 5M
Optics	Zeiss Discovery Stereo Microscope
Image FOV	488 x 2456 pixels
Image Scale	89.3481 pixel mm^{-1}
Imaging Rate	3 Hz